

First Limits on Axion Dark Matter from a DALI Prototype

Javier De Miguel^{1,2,3,*}, Enrique Joven¹, Elvio Hernández-Suárez¹, Juan F. Hernández-Cabrera¹, Haroldo Lorenzo-Hernández¹, Dylan Carroll⁴, Roger J. Hoyland¹, Edgar S. Carlin^{1,2}, Antonios Gardikiotis^{5,6}, Abaz Kryemadhi⁷, J. Daniel Marrero-Falcón², Marios Moroudas⁸, Chiko Otani³, J. Alberto Rubiño-Martín^{1,2}, and Konstantin Zioutas⁵

¹*Instituto de Astrofísica de Canarias, E-38200 La Laguna, Tenerife, Spain*

²*Departamento de Astrofísica, Universidad de La Laguna, E-38206 La Laguna, Tenerife, Spain*

³*RIKEN Center for Advanced Photonics, 519-1399 Aramaki-Aoba, Aoba-ku, Sendai, Miyagi 980-0845, Japan*

⁴*Independent researcher (unaffiliated); present address: Sagittal Optics, 38002 Santa Cruz de Tenerife, Spain*

⁵*Physics Department, University of Patras, GR 26504, Patras-Rio, Greece*

⁶*Institute of Quantum Computing and Quantum Technology,*

National Centre for Scientific Research “Demokritos”, 153 41 Athens, Greece

⁷*Computing, Math & Physics, Messiah University, Mechanicsburg, PA 17055, USA and*

⁸*Institute for Experimental Physics, University of Hamburg, 22761 Hamburg, Germany*

(The DALI Collaboration)

(Dated: March 24, 2026)

We report a pilot dark-matter search with a cryogenic, magnetized, scaled-down DALI prototype. An analysis of 36 hours of data reveals no statistically significant excess attributable to axionlike particles. We therefore set new exclusion limits in the 6.883–6.920 GHz band, reaching an axion–photon coupling sensitivity of $g_{a\gamma\gamma} \lesssim 1.27 \times 10^{-11} \text{GeV}^{-1}$ at 28.54 μeV . These results consolidate the DALI approach and motivate a next-stage haloscope to explore a broader mass range with upgraded instrumentation.

Introduction. Axions were proposed to address the quantum chromodynamics (QCD) problem of charge-conjugation and parity symmetry in the strong interaction [1]. Both axions [2, 3] and axionlike particles beyond the QCD framework—hereafter collectively referred to as axions—have long been hypothesized to constitute dark matter (DM) [4–7], an elusive substance whose existence is supported by indirect evidence [8]. Exploiting the weak coupling of axions to standard particles, various experimental methods have been developed to search for DM—see Refs. [9, 10] for a review.

The axion–photon interaction is described by the effective Lagrangian density

$$\mathcal{L} \supset g_{a\gamma\gamma} a \mathbf{E} \cdot \mathbf{B}, \quad (1)$$

where $g_{a\gamma\gamma}$ denotes the axion–photon coupling, a is the axion field, \mathbf{E} represents the electric field of the photon, and \mathbf{B} is an external static magnetic field that supplies the virtual photon required for Primakoff conversion [11]. A promising experimental approach to probing this interaction is the haloscope, first proposed by Sikivie [12], which in its most common implementation employs a magnetized resonant cavity to enhance the weak microwave signal induced by virialized axions in the Galactic halo. Despite several decades of development, the cavity haloscope faces increasing challenges in maintaining high sensitivity at progressively higher frequencies, as wave coherence requirements reduce the effective detection volume and thus the achievable sensitivity. In this

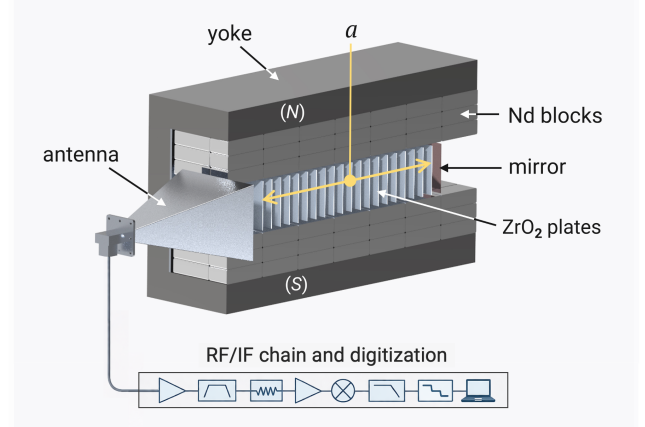


FIG. 1. Schematic view of the DALI(PoP) prototype. A tunnel yoke holds an array of Nd blocks that generates a dipole-like magnetic field. Ambient axions are converted into microwave photons, which are collected by the antenna. The resonator, composed of 20 ZrO_2 layers and enclosed by a copper mirror, enhances the weak axion-induced signal to an observable level. The detected signal is subsequently processed by the readout chain shown below (from left to right: amplifier, band-pass filter, attenuator, amplifier, downconverter, low-pass filter, analog-to-digital converter, and data storage). The haloscope is housed in a Faraday cage to suppress external spurious signals (not shown). The magnet is segmented along its longitudinal axis.

manuscript we report the first results from a demonstrator of the Dark-photons & Axion-Like particles Interferometer (DALI), a new-generation DM haloscope designed to complement axion searches at high frequencies. DALI [13–18] features a novel experimental setup for de-

* jdemiguel@iac.es

tecting wavelike DM, known as a *magnetized phased array* (MPA). A resonator placed in a static magnetic field enhances the faint signal expected from cosmic axions, for which a tunable Fabry–Pérot (FP) interferometer is employed [19]. In the MPA haloscope, the phased array forms a coherent electromagnetic pattern that couples to the resonant field of the FP tuner, thereby collecting the signal over the full open-cavity aperture. Interestingly, the resonance frequency is decoupled from the transverse area of the ceramic plates, allowing the resonator cross

section to be scaled independently of frequency. As a result, this architecture offers a complementary path toward resonant axion searches at higher frequencies, where maintaining large effective volumes and high sensitivity becomes increasingly challenging for conventional cavity haloscopes. Notably, DALI relies on mature, readily available components, enabling rapid, cost-effective deployment; the use of a conventional solenoid-type superconducting magnet, widely deployed in the medical industry, further reduces technical risk and facilitates procurement.

$$g_{a\gamma\gamma} \gtrsim 2.04 \times 10^{-11} \text{ GeV}^{-1} \left(\frac{\text{SNR}}{3}\right)^{1/2} \left(\frac{10^3}{Q_L}\right)^{1/2} \left(\frac{1+\beta}{\beta}\right)^{1/2} \left(\frac{100 \text{ cm}^2}{A}\right)^{1/2} \times \left(\frac{m_a}{50 \text{ } \mu\text{eV}}\right)^{5/4} \left(\frac{1 \text{ day}}{t}\right)^{1/4} \left(\frac{T_{\text{sys}}}{50 \text{ K}}\right)^{1/2} \frac{0.6 \text{ T}}{B} \left(\frac{0.45 \text{ GeV cm}^{-3}}{\rho_a}\right)^{1/2}. \quad (2)$$

The DALI program comprises different stages. As part of its scientific plan, in this work we report a proof-of-principle (PoP) test, at a lower scale, designed to retain a part of DALI’s physics potential while relieving hardware heaviness. The rest of this Letter is structured as follows. The section *Experimental setup* describes the DALI(PoP) prototype employed to search for axion DM, while *Data analysis* details the observations and their statistical treatment. A new limit on the DM axion parameter space is presented in *Results*.

Experimental setup. A schematic view of the DALI(PoP) prototype hosted at the IAC facilities at latitude $28^\circ 28' 29''$ N and longitude $16^\circ 18' 37''$ W is shown in Fig. 1. The apparatus can operate in two frequency ranges, 6–8 GHz and ~ 30 –40 GHz. The PoP prototype scales down DALI by approximately halving the number of layers of the FP tuner and reducing the plate size to $\sim 1:10$, which diminishes the detection cross-sectional area by ~ 100 . Thus, while the full-scale MPA is designed to cover larger cross-sectional areas by means of a phased array in which multiple antennas combine coherently, the reduced surface of the prototype can be covered with a single antenna while preserving the same DALI operating principle.

A detailed derivation for the DALI formalism is given in Refs. [14, 18]. The on-resonance axion-induced signal power in a DALI magnetized interferometer scales as $P_a \propto g_{a\gamma\gamma}^2 B^2 A Q_L \beta / (1 + \beta)$, where A represents the effective cross-sectional area, Q_L denotes the loaded quality factor, B is the external static magnetic field, and β accounts for receiver coupling. Combining this scaling with the Dicke radiometer relation [20], $\text{SNR} \propto P_a T_{\text{sys}}^{-1} (t / \Delta\nu_a)^{1/2}$, with T_{sys} the system noise temperature and $\Delta\nu_a$ the signal linewidth, yields the sensitivity law in Eq. 2; where m_a is the axion mass, t is the integration time, and ρ_a denotes the local density of DM, set at $0.45_{-0.09}^{+0.03} \text{ GeV cm}^{-3}$ [21] under the assumption that

the axion is its fundamental component.

In the DALI(PoP) haloscope, the superconducting solenoid of the full-scale DALI design is replaced by a lighter permanent-magnet assembly consisting of two sets of 36 grade-N44 neodymium (Nd) alloy blocks, each measuring $100 \times 100 \times 30$ mm, for a total of 24 three-magnet

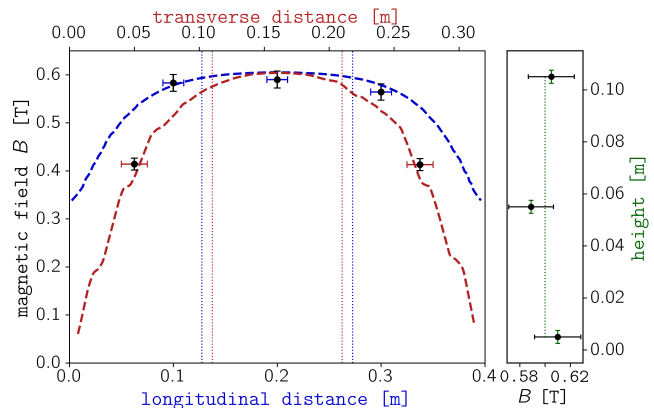


FIG. 2. Field simulation *vs.* measurements. The magnet bore is approximately 30 (transverse) \times 11 (height) \times 40 (longitudinal) cm. Two one-dimensional profiles are extracted from the 3D magnetic-field simulations: a center-longitudinal cut at half height (blue dashed) and a center-transverse cut (red dashed). The field generated by the magnets installed inside the steel yoke was simulated using Elmer FEM [22], employing Gmsh [23] to generate the three-dimensional meshes. The dotted lines indicate the resonator size ($10 \times 10 \times 14.5$ cm) in its centered configuration, shown for reference. Control Hall-probe measurements are shown with 3% vertical error bars and horizontal probe-positioning bars; the right inset displays three measurements along the bore height at the longitudinal center. The simulated field distribution is in good agreement with the measurements.

stacks, 12 at each pole, enclosed in a tunnel-yoke made of F-114 steel sheets with length, width, and height of about 1/2 m and a bore of approximately 30×11 cm. The magnetic field exhibits $\gtrsim 95\%$ homogeneity over the resonator volume, as measured with a HIRST-GM08 Hall-effect sensor, with a field strength of 0.59 ± 0.01 T—see Fig. 2. We employed a FP resonator composed of 20 layers of yttria-stabilized zirconia (ZrO_2), each of size 100×100 mm with ± 0.5 mm tolerance, thickness 1 ± 0.03 mm, and surface roughness below $0.1 \mu\text{m}$; the material has permittivity $\epsilon_r \sim 30$ and dielectric loss tangent $\tan \delta \sim 10^{-4}$ at centimeter wavelengths. In this pilot run, the plate spacing is fixed for a single frequency step at 6.21 ± 0.05 mm. The loaded quality factor was measured following the laboratory procedure described in Ref. [17] with a Rohde & Schwarz ZNB 20 vector network analyzer (VNA). For the present resonator stack, with an inter-plate spacing of $\sim \lambda/8$ (where λ is the wavelength), the response peaks at $Q_L \approx 2200$ near 6.907 GHz and follows a pseudo-Lorentzian profile, as shown in Fig. 3. Microwave absorbers are used to buffer against spillover and suppress reflections—EA-PF3000-24 and 3650-40-ML. A WR-137 standard horn antenna receives the signal, which is sent to a high electron mobility transistor radiometer composed of a cryogenic LNF-LNC4-8C low-noise amplifier (LNA), with ~ 40 dB gain and a noise temperature of a few kelvin, and a room-temperature backend with a second LNF-LNC4-8C, a 12 dB attenuator (Mini-Circuits® model 15542) to avoid compression at the second gain stage, and ~ 6 –8 GHz band-pass filtering. Powered by two closed-cycle ^4He cryocoolers, the system temperature was determined with the standard Y-factor method by heating a microwave absorber with a resistor (Ohmite HS100 330R J) over $\Delta T \sim 60$ K, yielding $T_{\text{sys}} \simeq 59$ K

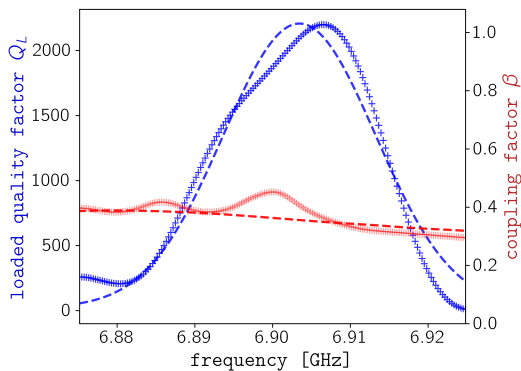


FIG. 3. Quality factor and coupling factor. Measured quality factor data is shown in blue. The full width at half maximum for a fit, represented by a blue dashed line, is ~ 20 MHz. In the present prototype configuration the receiver is undercoupled. The observed optical power coupling factor β is depicted in red, while broadband data (~ 5 –8 GHz) is smoothed with a SG baseline using a window size $W = 201$ and polynomial order $d = 1$, shown by a red dashed line as a reference. Throughout this work, Q_L and β are taken from the measured data, not from the fitted or smoothed curves.

for the present implementation, including contributions from the antenna temperature (49.3 K, cooling-limited under the >200 kg magnet load) and the receiver noise (9.7 K).

The larger receiving aperture of the WR-137 horn encompasses the effective cross-section entering Eq. 2, namely $A \simeq 100 \text{ cm}^2$. The antenna coupling is extracted from free-space VNA measurements; the resulting $\beta < 1$ (see Fig. 3) reflects an undercoupled antenna–resonator arrangement, leaving room for improved matching in future realizations. The instrumental parameters and uncertainties for this run are listed in Table I.

TABLE I. Uncertainties are weighted according to their order in Eq. 2 to estimate the propagated cumulative uncertainty in this run.

Parameter	Measured Uncertainty	
Quality factor (Q_L) [peak]	2198	8%
Coupling (β) [max.]	0.45	1%
Cross-section (A)	100 cm^2	1%
System temperature (T_{sys})	59.0 K	2%
Magnetic field (B)	0.59 T	3%
Propagation to $g_{a\gamma\gamma}$ sens.		5%

Components near the magnet are made of non-magnetic materials or placed where the fringe field is negligible. The cryostat is enclosed within a Faraday cage from Holland Shielding Systems B.V., equipped with a connector plate fitted with radio-frequency (RF) filters, waveguides, and ventilation honeycombs, to attenuate spurious microwave signals from outside by more than 60 dB. The data acquisition system (DAS) is built outside the shielding tent and consists of a zero intermediate frequency (ZIF) downconverter model thinkRFTM R5550-408, a two-channel digitizer, and a local server-based storage system. The downconverter shifts the radiometer output from RF to baseband, creating in-phase and quadrature (IQ) outputs for instantaneous acquisition of the full band, with a minor loss of data close to zero hertz. The IQ outputs pass through SLP-36+ low-pass filters with a nominal -3 dB cutoff frequency of approximately 40 MHz before simultaneous digitization. A mask balances the I and Q signals in amplitude and phase before channel combination, calibrated with a swept VNA measurement at the input of the ZIF downconverter. Direct acquisition of the IQ baseband signal is enabled by a dual-channel, 14-bit analog-to-digital converter (GaGe CSE8329). The digitized raw signals are continuously streamed to the local storage system via a peripheral component interconnect express link, where the 14-bit analog-to-digital converter output is recorded in 16-bit integer format and can store up to 18 TB of time-domain samples for subsequent post-processing.

Data analysis. Data were acquired for 36 hours effective time between February 17th and March 5th, 2026, using the equipment described in the previous section. A

total of $N=12960$ spectra were recorded at 125 MS/s, centered at 6.90 GHz. Each stored spectrum corresponds to the average of 9540 consecutive dual-channel fast Fourier transform (FFT) segments of length 2^{17} samples, yielding an effective integration time of 10 s per file and a frequency resolution of $\Delta\nu_b \simeq 954$ Hz. In total, this corresponds to approximately 64.8 TB of raw time-domain data, compressed to 44.2 GB in the stored frequency-domain dataset.

In Ref. [15], we adapted the analysis method of Ref. [24] to our MPA haloscope and used the resulting pipeline to perform end-to-end Monte Carlo (MC) simulations, in which a synthetic axion signal was injected into a noisy background and its detection rate was used to fine-tune the sensitivity (prefactor in Eq. 2); thus accounting for the finite-bin and line-shape effects of the analysis. In this section, we follow the methodology and nomenclature introduced there. First, time-to-frequency domain conversions were calculated using the **Fastest Fourier Transform in the West** library [25], and then spectra were cropped within the threshold $Q_L > 250$, chosen to retain the sensitive resonant band. Cropped spectra were averaged in the frequency domain and the resulting spectrum was smoothed using a median kernel with a window size $W = 51$. In this stage of the pipeline, prominent spurious interferences were flagged as any signal exceeding 7 times the average; the compromised bins are flagged and iteratively replaced by random values drawn from a Gaussian distribution with the same mean and standard deviation as the values of the average spectrum until no further compromised bins are identified [26]. The corresponding bins of the individual spectra are also replaced with random values in the same manner; these bins are subsequently masked in the analysis. Residual broad spectral structure in each spectrum was then removed using a Savitzky–Golay (SG) baseline with $W = 51$ and polynomial degree $d = 6$. Processed spectra were now weighted by the Q factor at each bin. Rescaled spectra were then combined and the stacked spectrum was rebinned with parameters $K_r = 8$, $K_g = 3$, and $z = 0.65$, such that the axion-induced linewidth spans $\sim K_r K_g / 3$ bins. The resulting grand spectrum (GS), with frequency-bin width $\Delta\nu_{GS} = K_r \Delta\nu_b \approx 8$ kHz, is obtained from a weighted sum that accounts for the expected axion line shape in the laboratory frame,

$$f(v) = \frac{2}{\sqrt{\pi}} \left(\sqrt{\frac{3}{2}} \frac{1}{r v_a \langle \beta_{\text{rms}}^2 \rangle} \right) \sinh \left(\frac{3r}{\sqrt{2}} \frac{(v - v_a)}{v_a \langle \beta_{\text{rms}}^2 \rangle} \right) \times \exp \left[-\frac{3}{2} \left(\frac{(v - v_a)}{v_a \langle \beta_{\text{rms}}^2 \rangle} \right)^2 - \frac{3r^2}{2} \right], \quad (3)$$

where v is the axion velocity in the lab frame, v_a is the mean axion velocity in the Galactic rest frame, $r \equiv v_{\text{lab}}/v_{\text{rms}}$ encodes the lab motion relative to the halo, and $\langle \beta_{\text{rms}}^2 \rangle = 3/2 v_{\text{rms}}^2/c^2$ is the mean squared velocity in units of the speed of light c , with $v_{\text{rms}} \simeq 270$ km/s. The total lab-frame velocity is $v_{\text{lab}} = v_{\odot} + v_{\oplus} + v_R$,

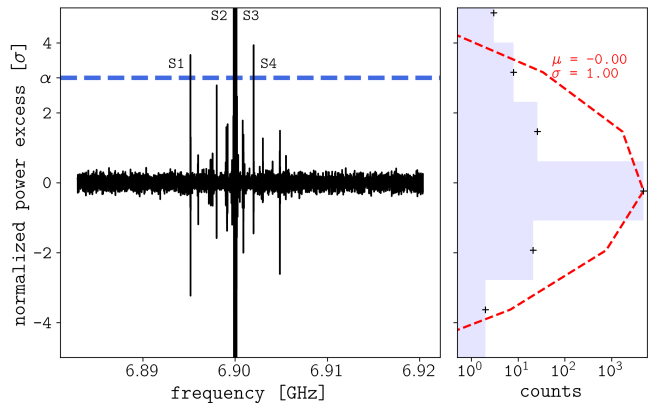


FIG. 4. Normalized, correlation-corrected grand spectrum (left), with detection threshold $\alpha = 3$ (blue). Narrow gaps indicate masked frequency bins identified from dedicated interference-control data. We label the four main masked regions as S1–S4, all attributed to instrumental origin—cf. Table II. Inset: histogram of normalized power excesses with the best-fitting Gaussian (red dashed), showing its mean (μ) and standard deviation (σ).

where $v_{\odot} \simeq 230$ km/s is the Sun’s velocity relative to the Galactic frame, $v_{\oplus} \simeq 29.8$ km/s is Earth’s orbital speed, and $v_R = \omega_{\oplus} R_{\oplus} \cos \phi_{\text{det}}$ accounts for Earth’s rotation at detector latitude ϕ_{det} , with $\omega_{\oplus} = 2\pi/\text{day}$ and $R_{\oplus} \simeq 6371$ km the Earth’s equatorial radius [24]. The filter-induced correlations among bins in the normalized GS were corrected at first order by dividing by its standard deviation. Candidates are then flagged as the bins exceeding a significance threshold (α) for an arbitrary confidence level (CL) assuming a normal distribution as $\alpha = \text{SNR} - \text{CL}$.

Narrow spectral features not removed by the upstream screening can nevertheless become significant only at the GS stage, where persistent lines accumulate through stacking, rebinning, and line-shape weighting. Bootstrap MC simulations of the processed data show short-range correlations in the normalized GS extending over approximately three bins. Accordingly, the regions S1–S4 in Fig. 4 denote the final masked windows used in the analysis, obtained by extending each above-threshold GS bin to its adjacent ± 3 bins. Dedicated control acquisitions show that the above-threshold excesses are instrumental in origin. Persistent narrow lines are observed un-

TABLE II. Masked regions in the normalized, correlation-corrected GS, with frequency and mass intervals, significance (sig.), and most plausible instrumental origin (IF or RF).

Region	Frequency [GHz]	Mass [μeV]	Sig. [σ]	Origin
S1	6.895140–6.895185	28.5160–28.5162	3.66	RF
S2	6.899834–6.900048	28.5354–28.5363	31.15	IF
S3	6.900079–6.900178	28.5364–28.5368	12.11	IF
S4	6.901987–6.902033	28.5443–28.5445	3.94	RF?

der otherwise identical digitization and FFT conditions with the RF input from the cryogenic front-end disconnected and the room-temperature RF chain terminated with a matched load; additional short reference-load acquisitions are consistent with the same interpretation. Control runs with the RF center frequency shifted by +50 MHz support the following classification: S2 is identified as an IF spur, S3 is also likely IF-related, S1 is more plausibly associated with RF pickup, and S4 is likewise compatible with RF interference—see Table II. The masked regions appear as narrow gaps in Fig. 5.

Results. The main results of this work are depicted in Fig. 5. We analyzed 12960 files of 10.0 s each (total integration time 36.0 h) in the 6.882934–6.920361 GHz band (28.466–28.621 μeV), with a robust (9-bin averaged) peak sensitivity of $g_{a\gamma\gamma} \simeq 1.27 \times 10^{-11} \text{ GeV}^{-1}$ near 6.901 GHz (28.54 μeV), and excluded axions at 90% CL in all GS bins except for the narrow ranges listed in Table II (52 of 4904 bins, $\sim 1\%$ of the GS).

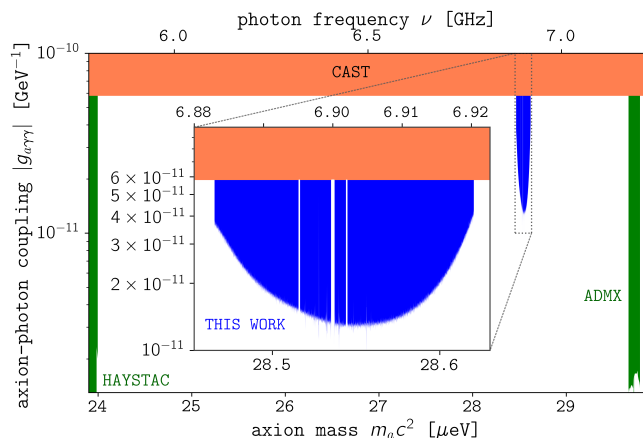


FIG. 5. New exclusion region (blue) at 90% CL. Narrow gaps indicate masked bins and vetoed neighborhoods around above-threshold excursions (Table II). Other laboratory-based constraints in the vicinity of the newly excluded region are also shown [27–30].

This proof-of-concept test establishes new exclusion

limits, marks a first step toward broadband operation of the DALI(PoP) prototype, and lays the groundwork for the full-scale DALI experiment, designed to complement existing axion DM searches by probing a region of parameter space that, while well motivated by postinflationary scenarios, remains poorly explored because QCD-axion searches at high frequencies are technically challenging.

Acknowledgements. The project that gave rise to these results received the support of a fellowship from “la Caixa” Foundation (ID 100010434). The fellowship code is LCF/BQ/PI24/12040023”. J.D.M. acknowledges support from the Spanish Ministry of Science, Innovation and Universities and the Agency (EUR2024-153552 financed by MICIU/AEI/10.13039/501100011033). We gratefully acknowledge financial support from the Severo Ochoa Program for Technological Projects and Major Surveys 2020-2023 under Grant No. CEX2019-000920-S; Recovery, Transformation and Resiliency Plan of Spanish Government under Grant No. C17.I02.CIENCIA.P5; Operational Program of the European Regional Development Fund (ERDF) under Grant No. EQC2019-006548-P; IAC Plan de Actuación 2022. J.F.H.-C. was supported by the Resident Astrophysicist Programme of the Instituto de Astrofísica de Canarias. This work was supported by the RIKEN’s program for Special Postdoctoral Researchers (SPDR). M.M. acknowledges funding by the Deutsche Forschungsgemeinschaft (DFG, German Research Foundation) under Germany’s Excellence Strategy—EXC 2121 “Quantum Universe”—390833306. Thanks to J. Potticary and R. Barreto for technical support.

Data availability. The source data and code used to generate the plots in this paper are available from the corresponding author upon reasonable request.

Author contribution statements. J.D.M., E.J., E.H.-S., J.F.H.-C., H.L.-H., and D.C. conceived, designed and built the prototype. J.D.M., E.J., and D.C. installed and operated the detector. J.D.M. and E.J. organized the data-taking runs and general operation of the experiment, coordinated and monitored the data taking. J.D.M. supervised the project, processed and analyzed the data, and led the article drafting and editing with input from all authors. All authors provided critical feedback and helped shape the research, analysis, and manuscript.

[1] R. D. Peccei and H. R. Quinn, CP conservation in the presence of pseudoparticles, *Phys. Rev. Lett.* **38**, 1440 (1977).
 [2] S. Weinberg, A new light boson?, *Phys. Rev. Lett.* **40**, 223 (1978).
 [3] F. Wilczek, Problem of strong p and t invariance in the presence of instantons, *Phys. Rev. Lett.* **40**, 279 (1978).
 [4] F. Zwicky, Die Rotverschiebung von extragalaktischen Nebeln, *Helvetica Physica Acta* **6**, 110 (1933).
 [5] L. Abbott and P. Sikivie, A cosmological bound on the invisible axion, *Physics Letters B* **120**, 133 (1983).

[6] M. Dine and W. Fischler, The not-so-harmless axion, *Physics Letters B* **120**, 137 (1983).
 [7] J. Preskill, M. B. Wise, and F. Wilczek, Cosmology of the invisible axion, *Physics Letters B* **120**, 127 (1983).
 [8] V. C. Rubin and J. Ford, W. Kent, Rotation of the Andromeda Nebula from a Spectroscopic Survey of Emission Regions, *Astrophysical Journal* **159**, 379 (1970).
 [9] A. Arza *et al.*, The COSMIC WISPerS White Paper: The physics case for Weakly Interacting Slim Particles, arXiv:2603.03433 [hep-ph].
 [10] B. Andrieu *et al.*, Enhancing European Coopera-

- tion in the Search for Dark Matter, arXiv (2025), [arXiv:2504.01688](https://arxiv.org/abs/2504.01688) [hep-ex].
- [11] H. Primakoff, Photoproduction of neutral mesons in nuclear electric fields and the mean life of the neutral meson, *Phys. Rev.* **81**, 899 (1951).
- [12] P. Sikivie, Experimental Tests of the “Invisible” Axion, *Phys. Rev. Lett.* **51**, 1415 (1983).
- [13] J. De Miguel, A dark matter telescope probing the 6 to 60 GHz band, *Journal of Cosmology and Astroparticle Physics* **2021** (04), 075.
- [14] J. De Miguel, J. F. Hernández-Cabrera, E. Hernández-Suárez, E. Joven-Álvarez, C. Otani, and J. A. Rubiño-Martín (DALI), Discovery prospects with the Dark-photons & Axion-like particles Interferometer, *Phys. Rev. D* **109**, 062002 (2024), [arXiv:2303.03997](https://arxiv.org/abs/2303.03997) [hep-ph].
- [15] J. F. Hernández-Cabrera, J. De Miguel, E. J. Álvarez, E. Hernández-Suárez, J. A. Rubiño Martín, and C. Otani, A Forecast of the Sensitivity of the DALI Experiment to Galactic Axion Dark Matter, *Symmetry* **16**, 163 (2024), [arXiv:2310.20437](https://arxiv.org/abs/2310.20437) [hep-ph].
- [16] J. F. Hernández-Cabrera, J. De Miguel, E. Hernández-Suárez, E. Joven-Álvarez, H. Lorenzo-Hernández, C. Otani, M. A. Rapado-Tamarit, and J. A. Rubiño-Martín, Experimental measurement of the quality factor of a Fabry-Pérot open-cavity axion haloscope, *Journal of Instrumentation* **19** (1), P01022, [arXiv:2310.16013](https://arxiv.org/abs/2310.16013) [hep-ph].
- [17] J. F. Hernández-Cabrera, J. De Miguel, E. Hernández-Suárez, E. Joven, C. Otani, J. A. Rubiño Martín, and K. Zioutas (DALI Collaboration), Echo-free quality factor of a multilayer axion haloscope, *Phys. Rev. D* **110**, 072013 (2024).
- [18] J. De Miguel, A. Kryemadhi, and K. Zioutas (DALI), DALI sensitivity to streaming axion dark matter, *Phys. Rev. D* **111**, 023016 (2025), [arXiv:2404.13970](https://arxiv.org/abs/2404.13970) [hep-ph].
- [19] A. Perot and C. Fabry, On the Application of Interference Phenomena to the Solution of Various Problems of Spectroscopy and Metrology, *Astrophysical Journal* **9**, 87 (1899).
- [20] R. H. Dicke, The Measurement of Thermal Radiation at Microwave Frequencies, *Review of Scientific Instruments* **17**, 268 (1946).
- [21] P. G. Staudt, J. S. Bullock, M. Boylan-Kolchin, A. Wetzel, and X. Ou, Sliding into DM: Determining the local dark matter density and speed distribution using only the local circular speed of the Galaxy, (2024), [arXiv:2403.04122](https://arxiv.org/abs/2403.04122) [astro-ph.GA].
- [22] Elmer fem – open source multiphysical simulation software, last visited 10 June 2024.
- [23] Gmsh: a three-dimensional finite element mesh generator with built-in pre- and post-processing facilities, last visited 10 June 2024.
- [24] B. M. Brubaker, L. Zhong, S. K. Lamoreaux, K. W. Lehnert, and K. A. van Bibber, HAYSTAC axion search analysis procedure, *Phys. Rev. D* **96**, 123008 (2017).
- [25] M. Frigo and S. Johnson, The design and implementation of fftw3, *Proceedings of the IEEE* **93**, 216 (2005).
- [26] A. Quiskamp, B. T. McAllister, P. Altin, E. N. Ivanov, M. Goryachev, and M. E. Tobar, Direct search for dark matter axions excluding alp cogenesis in the 63 to 67 μeV range with the organ experiment, *Science Advances* **8**, eabq3765 (2022), <https://www.science.org/doi/pdf/10.1126/sciadv.abq3765>.
- [27] K. Altenmüller, V. Anastassopoulos, S. Arguedas-Cuendis, S. Aune, J. Baier, K. Barth, H. Bräuninger, G. Cantatore, F. Caspers, J. F. Castel, S. A. Çetin, F. Christensen, C. Cogollos, T. Dafni, M. Davenport, T. A. Decker, K. Desch, D. Díez-Ibáñez, B. Döbrich, E. Ferrer-Ribas, H. Fischer, W. Funk, J. Galán, J. A. García, A. Gardikiotis, I. Giomataris, J. Golm, C. H. Hailey, M. D. Hasinoff, D. H. H. Hoffmann, I. G. Irastorza, J. Jacoby, A. C. Jakobsen, K. Jakovčić, J. Kaminski, M. Karuza, S. Kostoglou, C. Krieger, B. Lakić, J. M. Laurent, G. Luzón, C. Malbrunot, C. Margalejo, M. Maroudas, L. Miceli, H. Mirallas, P. Navarro, L. Obis, A. Özbey, K. Özbozduman, T. Papaevangelou, O. Pérez, M. J. Pivovarov, M. Rosu, E. Ruiz-Chóliz, J. Ruz, S. Schmidt, M. Schumann, Y. K. Semertzidis, S. K. Solanki, L. Stewart, T. Vafeiadis, J. K. Vogel, and K. Zioutas (CAST Collaboration), New upper limit on the axion-photon coupling with an extended cast run with a xe-based micromegas detector, *Phys. Rev. Lett.* **133**, 221005 (2024).
- [28] L. Zhong, S. Al Kenany, K. M. Backes, B. M. Brubaker, S. B. Cahn, G. Carosi, Y. V. Gurevich, W. F. Kindel, S. K. Lamoreaux, K. W. Lehnert, S. M. Lewis, M. Malnou, R. H. Maruyama, D. A. Palken, N. M. Rapidis, J. R. Root, M. Simanovskaia, T. M. Shokair, D. H. Speller, I. Urdinaran, and K. A. van Bibber, Results from phase 1 of the haystac microwave cavity axion experiment, *Phys. Rev. D* **97**, 092001 (2018).
- [29] B. M. Brubaker, L. Zhong, Y. V. Gurevich, S. B. Cahn, S. K. Lamoreaux, M. Simanovskaia, J. R. Root, S. M. Lewis, S. Al Kenany, K. M. Backes, I. Urdinaran, N. M. Rapidis, T. M. Shokair, K. A. van Bibber, D. A. Palken, M. Malnou, W. F. Kindel, M. A. Anil, K. W. Lehnert, and G. Carosi, First results from a microwave cavity axion search at 24 μeV , *Phys. Rev. Lett.* **118**, 061302 (2017).
- [30] C. Boutan, M. Jones, B. H. LaRoque, N. S. Oblath, R. Cervantes, N. Du, N. Force, S. Kimes, R. Ottens, L. J. Rosenberg, G. Rybka, J. Yang, G. Carosi, N. Woollett, D. Bowring, A. S. Chou, R. Khatiwada, A. Sonnenschein, W. Wester, R. Bradley, E. J. Daw, A. Agrawal, A. V. Dixit, J. Clarke, S. R. O’Kelley, N. Crisosto, J. R. Gleason, S. Jois, P. Sikivie, I. Stern, N. S. Sullivan, D. B. Tanner, P. M. Harrington, and E. Lentz (ADMX Collaboration), Piezoelectrically tuned multimode cavity search for axion dark matter, *Phys. Rev. Lett.* **121**, 261302 (2018).